Inorg. Chem. **2008**, *47*, 11774−11782

The Crystal Chemistry of Ferric Oxyhydroxyapatite

H. R. Low,*,† N. Phonthammachai,† A. Maignan,‡ G. A. Stewart,§ T. J. Bastow,|| L. L. Ma,† and T. J. White†

School of Materials Science and Engineering, Nanyang Technological University, 50 Nanyang Avenue, Singapore 639798, Laboratoire CRISMAT, UMR CNRS 6508, ENSICAEN, 6 Bd du Marechal Juin, 14050 Caen, Cedex, France, School of Physical, Environmental and Mathematical Sciences, University of New South Wales at the Australian Defence Force Academy, Canberra ACT 2600, Australia, and CSIRO Materials Science and Engineering, Private Bag 33, Clayton South, VIC 3169, Australia

Received August 6, 2008

Ferric hydroxyapatites (Fe-HAp) and oxyapatites (Fe-OAp) of nominal composition $[Ca_{10-x}Fe_x^{3+}][(PO_4)_6][(OH)_{2-x}O_x]$ ($0 \leq x \leq 0.5$) were synthesized from a coprecipitated precursor calcined under flowing nitrogen. The solid solubility of iron was temperature-dependent, varying from $x = 0.5$ after firing at 600 °C to $x \sim 0.2$ at 1000 °C, beyond which Fe-OAp was progressively replaced by tricalcium phosphate (Fe-TCP). Crystal size (13−116 nm) was controlled by iron content and calcination temperature. Ferric iron replaces calcium by two altervalent mechanisms in which carbonate and oxygen are incorporated as counterions. At low iron loadings, carbonate predominantly displaces hydroxyl in the apatite channels ($Ca^{2+} + OH^- \rightarrow Fe^{3+} + CO_3^{2-}$), while at higher loadings, "interstitial" oxygen is tenanted in the framework ($2Ca^{2+} + \square_{vac} \rightarrow 2Fe^{3+} + O^{2+}$). Although Fe^{3+} is smaller than Ca^{2+}, the unit cell dilates as iron enters apatite, providing evidence of oxygen injection that converts PO_4 tetrahedra to PO_5 trigonal bipyramids, leading to the crystal chemical formula $[Ca_{10-x}Fe_x][(PO_4)_{6-x/2}(PO_5)_{x/2}][(OH)_{2-y}O_{2y}]$ ($x \leq 0.5$). A discontinuity in unit cell expansion at $x \sim 0.2$ combined with a substantial reduction of the carbonate FTIR fingerprint shows that oxygen infusion, rather than tunnel hydroxyl displacement, is dominant beyond this loading. This behavior is in contrast to ferrous-fluorapatite where $Ca^{2+} \rightarrow Fe^{2+}$ aliovalent replacement does not require oxygen penetration and the cell volume contracts with iron loading. All of the materials were paramagnetic, but at low iron concentrations, a transition arising from crystallographic modification or a change in spin ordering is observed at 90 K. The excipient behavior of Fe-OAp was superior to that of HAp and may be linked to the crystalline component or mediated by a ubiquitous nondiffracting amorphous phase. Fe-HAp and Fe-OAp are not intrinsically suitable magnetic agents for drug delivery but may be useful in reactive cements that promote osteoblast proliferation.

Introduction

Hydroxyapatite [$Ca_{10}(PO_4)_6(OH)_2$, HAp] is the major inorganic constituent of bone and tooth enamel and is not only used as a clinical material[1] but can be adapted as a phosphor,[2] toxic metal waste form,[3] and catalyst.[4] It is the most widely studied compound of the extensive apatite family, whose members have primarily hexagonal $P6_3/m$ structures possessing the crystallochemical formula $[A^I_4][A^{II}_6][(BO_4)_6]X_2$, where A^I/A^{II} are discrete large cations, B is a metalloid, and X is an anion or oxyanion.[5,6] Apatites have zeolitic character in which a framework, which is constructed from columns of face-sharing A^IO_6 metaprisms corner-connected to BO_4 tetrahedra, creates one-dimensional tunnels occupied by counterions (Figure 1). The HAp framework has the ideal stoichiometry $[Ca^I_4(PO_4)_6]^{10-}$, with the channel containing $[Ca^{II}_6(OH)_2]^{10+}$. Biogenic apatites are

* Author to whom correspondence should be addressed. E-mail: HRLow@ntu.edu.sg.
† Nanyang Technological University.
‡ UMR CNRS 6508, ENSICAEN.
§ University of New South Wales.
|| CSIRO Materials Science and Engineering.

(1) Hertz, A.; Bruce, I. J. *Nanomedicine* **2007**, *2* (6), 899.
(2) Barbarand, J.; Pagel, M. *Am. Mineral.* **2002**, *86*, 473.
(3) Dong, Z. L.; White, T. J.; Wei, B.; Laursen, K. *J. Am. Ceram. Soc.* **2002**, *85*, 2515.
(4) Nishikawa, H.; Omamiuda, K. *J. Mol. Catal.* **2002**, *179*, 193.
(5) White, T. J.; Dong, Z. *Acta Crystallogr., Sect. B* **2003**, *59*, 1.
(6) Kay, M. I.; Young, R. A. *Nature* **1964**, *204*, 1050.

10.1021/ic801491t CCC: $40.75
Published on Web 11/14/2008

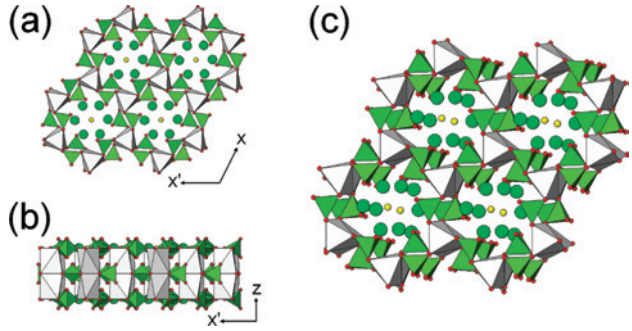

Figure 1. Structure drawings of $P6_3/m$ $[Ca^{I}_4Ca^{II}_6](PO_4)_6(OH)_2$ hydroxyapatite. (a) An [001] projection of the zeolitic $[Ca^{I}_4(PO_4)_6]^{10-}$ framework that is constructed from $Ca^{I}O_6$ metaprisms (gray polyhedra) and PO_4 tetrahedra (green polyhedra). The metaprism is a solid figure intermediate between an octahedron and trigonal prism. The one-dimensional channels are occupied by Ca^{II} (green cation) and OH (yellow oxyanion) that combine as $[Ca^{II}_6(OH)_2]^{10+}$ counterions. The framework is flexible, and during substitution of Ca, P, or OH by other species, the metaprisms twist cooperatively to dilate or constrict the channel according to the size and occupation factors of the substituents. (b) The [110] projection shows the alternation of twist along [001] between successive metaprisms and emphasizes the isolation of the PO_4 tetrahedra. (c) A clinographic projection of apatite illustrating the spatial relationship between the framework polyhedra and channel ions.

complex, with nonstoichiometry and chemical substitutions accommodated by topological distortion of the framework and charge-coupled ionic tenancy over the $A^{I}/A^{II}/X$ sites, at times with the concomitant replacement of (BO_4) by $(BO_3)/(BO_5)$ units.[7] The therapeutic functions of synthetic HAp are modified by adjusting crystal size and composition,[8] sometimes supplemented by the introduction of a coexisting amorphous phase.[9] Excipient properties are manipulated by inserting small cations (Si^{4+}, Fe^{3+}, Mg^{2+}, or Zn^{2+}) to regulate bioactivity,[10−13] but these have limited solid solubility in HAp, inhibit crystal growth, and when present at higher concentrations stabilize tricalcium phosphate (TCP).[14,15] Unambiguous characterization of these finely divided apatites is challenging and requires quantitative diffraction analyses supported by a spectroscopic investigation of metal bonding.

Iron-bearing HAp (Fe-HAp) is a component of bioglasses and biocements that accelerate bone regeneration,[16] and it has been suggested that magnetism might be exploited for drug delivery.[17] However, iron is not an obvious substituent in HAp, as the ferrous (ionic radius = 0.78 Å, for 6-coordination to oxygen) and ferric (ionic radius = 0.645 Å) species do not evidentially meet typically accepted bond valence criteria for insertion. While it is generally assumed that $Fe^{2+/3+}$ will replace Ca^{2+} (ionic radius = 1.00 Å),[18,19] the discrepancy in size is large, and mechanisms for altervalent charge balance when Fe^{3+} displaces Ca^{2+} have not been examined. Furthermore, "crystallochemical incorporation" in HAp is sometimes equated with "surface adsorption"[20] and "phosphate phase",[21] although these are clearly distinct, and the solid solubility and local environment of Fe^{3+} in HAp remain poorly defined, as single-phase products are difficult to synthesize. The valences of iron in HAp prepared using coprecipitation,[22] solid-state reaction,[23] and microwave irradiation[24] are reported, but less emphasis has been given to defining the crystallographic location and coordination of the metal.[25,26] In addition, the possible coexistence of Fe-HAp and ferric oxyapatite (Fe-OAp) with amorphous phases is rarely considered, although these are probably bioactive,[27] and where magnetic properties have been measured,[28,29] the materials were often polyphase.

In this investigation, ferric oxyhydroxyapatites were synthesized to their probable solid solution limits to better define crystal chemistry, locate the HAp-OAp-TCP phase boundary, and verify amorphous content. The magnetic properties and biocompatibility of the products were also examined.

Materials and Methods

Synthesis. Fe-Ap of nominal composition $[Ca_{10-x}Fe_x^{3+}][(PO_4)_6][(OH)_{2-x}O_x]$ $(0 \le x \le 0.5)$ was synthesized from stoichiometric proportions of the reagents, as preliminary experiments showed that higher iron contents lead to TCP as the dominant phase. A 0.1 M Fe^{3+} solution was prepared by dissolving 2.5 mmol of iron chloride tetrahydrate ($FeCl_2 \cdot 4H_2O$) in 25 mL of deionized water. This solution was stirred for 10 min at room temperature with an aqueous suspension of calcium hydroxide ($Ca(OH)_2$; 0.064 mol/128 mL). Phosphate crystallization was initiated by adding 0.2 M orthophosphoric acid (H_3PO_4) dropwise to the suspension (18 mL/min) with continuous mixing. The slurry was stirred at 65 °C for 90 min and maintained at 100 °C for a further 2 h before settling the precipitate at the ambient temperature. The product was separated using vacuum filtration and washed several times to remove excess chloride prior to drying overnight at 100 °C. All of these procedures were conducted in the air, resulting in the introduction of carbonate in a synergistic fashion with Fe^{3+},

(7) White, T. J.; Ferraris, C.; Kim, J.; Madhavi, S. *Rev. Mineral. Geochem.* **2005**, *57*, 307.
(8) Leventouri, Th. *Biomaterials* **2006**, *27*, 3339.
(9) LeGeros, R. Z.; LeGeros, J. P. *Phosphate Minerals* **1984**, 351.
(10) Leventouri, Th.; Bunaciu, C. E.; Perdikatsis, V. *Biomaterials* **2003**, *24*, 4205.
(11) Morrissey, R.; Rodriguez-Lorenzo, L. M.; Gross, K. A. *J. Mater. Sci.: Mater. Med.* **2005**, *16*, 387.
(12) Suchanek, W. L.; Byrappa, K.; Shuk, P.; Riman, R. E.; Janas, V. F.; TenHuisen, K. S. *Biomaterials* **2004**, *25*, 4647.
(13) Fujii, E.; Ohkubo, M.; Tsuru, K.; Hayakawa, S.; Osaka, A.; Kawabata, K.; Bonhomme, C.; Babonneau, F. *Acta Biomater.* **2006**, *2*, 69.
(14) Wang, J.; Nonami, T.; Yubata, K. *J. Mater. Sci.: Mater. Med.* **2008**, *19*, 2663.
(15) Okamoto, Y.; Hidaka, S. *J. Biomed. Mater. Res.* **1994**, *28*, 1403.
(16) Leventouri, Th.; Kis, A. C.; Thompson, J. R.; Anderson, I. M. *Biomaterials* **2005**, *26*, 4924.
(17) Pankhurst, Q. A.; Connolly, J.; Jones, S. K.; Dobson, J. *J Phys. D, Appl. Phys.* **2003**, *36*, R167.
(18) Jiang, M.; Terra, J.; Rossi, A. M.; Morales, M. A.; Saitovitch, E. M. B.; Ellis, D. E. *Phys. Rev. B: Condens. Matter Mater. Phys.* **2002**, *66*, 224107.
(19) Okazaki, M.; Takahashi, J. *Biomaterials* **1997**, *18*, 11.
(20) Wakamura, M.; Kandori, K.; Ishikawa, T. *Colloids Surf., A* **2000**, *164*, 297.
(21) Bauminger, E.; Ofer, S.; Gedalia, I.; Horowitz, G.; Mayer, I. *Calcif. Tissue Int.* **1985**, *37*, 386.
(22) Sutter, B.; Ming, D. W.; Clearfield, A.; Hossner, L. R. *Soil Sci. Soc. Am. J.* **2003**, *67*, 1935.
(23) Khudolozhkin, B. O.; Urusov, V. S.; Kurash, V. V. *Geochem. Int.* **1974**, *11*, 748.
(24) Weeraphat, P.; Siwaporn, M. *Int. J. Nanosci.* **2007**, *(6)1s*, 9.
(25) Ok, H. N. *Phys. Rev.* **1969**, *185*, 477.
(26) Mayer, I.; Diab, H.; Felner, I. *J. Inorg. Biochem.* **1992**, *45*, 129.
(27) Rey, C.; Hina, A.; Tofighi, A.; Glimcher, M. J. *Cells Mater.* **1995**, *5*, 345.
(28) Wu, H.; Wang, T.; Sun, J.; Wang, W.; Lin, F. *Nanotechnology* **2007**, *18*, 165601.
(29) Gross, K. A.; Jackson, R.; Cashion, J. D.; Rodriguez-Lorenzo, L. M. *Eur. Cell Mater.* **2002**, *3*, 114.

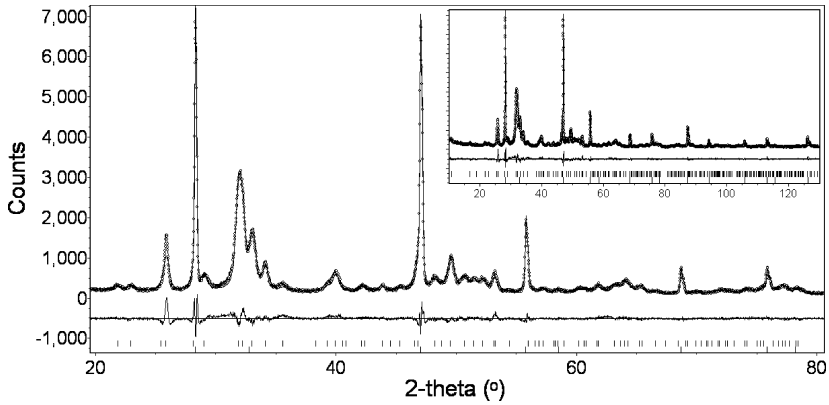

Figure 2. Rietveld plot of Fe-OAp ($x = 0.2$) prepared by sintering under N_2 (600 °C/2 h) and spiked with CaF_2 (20 wt %) to extract amorphous content. The upper trace is an overlay of the experimental pattern (○) and the calculated intensity shown as a continuous line. The lower trace contains the intensity differences between the experimental and calculated patterns. Bottom-most are the Bragg markers for Fe-OAp (upper) and CaF_2 (lower).

especially for $x \leq 0.3$ (as considered in the Discussion). This precursor was calcined (600−1000 °C) under nitrogen using a heating rate of 1 °C/min, a dwell time of 2 h, and finally a cooling rate of 5 °C/min. Sintering in the air was inappropriate, as this yielded a mixture of apatite and hematite (Fe_2O_3). Attempts to grow larger crystals by higher-temperature sintering and hydrothermal methods proved unsuccessful.

Quantitative Phase Analysis. Fe-Ap products were manually ground with an agate mortar and pestle prior to powder X-ray diffraction (XRD) with the pattern recorded using Ni-filtered Cu Kα radiation generated by a Shimadzu X-ray Diffractometer-6000 generator operating at 40 kV and 30 mA. Data were accumulated with a step scan increment of 0.02° 2θ and a dwell time of 2 s over the angular range 10−130°. All specimens were spiked with a silicon standard (10 wt %, NIST660a, $a = 5.40825$ Å) to determine the unit cell constants absolutely, while amorphous content was scaled against a standard addition of calcium fluoride (20 wt %), chosen to have an X-ray mass adsorption coefficient similar to HAp. Rietveld refinement was performed using the fundamental parameters approach, with TOPAS V3 (Bruker-AXS) and $P6_3/m$ hydroxyapatite[30] as the starting model (Figure 2). Crystallographic parameters were ultimately refined simultaneously, but initially, these variables were released in the sequence scale factor, zero shift, Chebyshev background polynomial (4th order), crystallite size (i.e., coherently scattering domain size), and lattice parameters. Phosphorus magic angle spinning nuclear magnetic resonance (^{31}P MAS NMR) spectra were acquired at 10 kHz with a Bruker Avance 400 NMR spectrometer using 85% H_3PO_4 as a primary standard at 0 ppm and ammonium dihydrogen phosphate (ADP) as a secondary standard at +0.9 ppm. Experimental resonances were fitted with Gaussian and Lorentzian lines using DMfit.[31] Powders were mixed with potassium bromide (KBr) and pressed into pellets prior to Fourier transform infrared (FTIR) absorption measurements performed over 16 scans in the wavenumber range of 400−4000 cm^{-1} with a Perkin-Elmer (Spectrum 2000) spectrophotometer. To differentiate crystallographic hydroxyl and carbonate from surface sorbed species, 30 mg of Fe-HAp was stirred with 30 mL of 0.05 M hydrochloric acid for 5 min, washed and centrifuged with deionized water, and oven-dried at 100 °C before acquiring the FTIR spectrum.[32]

Chemical State and Magnetism. ^{57}Fe−Mössbauer spectra were recorded at 300 K using a commercial drive unit and transducer (Wissel) operating in the sinusoidal oscillation mode with a 25 mCi source of ^{57}Co:Rh, and the 14.4 keV γ-rays were detected with a Kr proportional counter. The drive velocity was calibrated against the 300 K spectrum of α-Fe. Electron paramagnetic resonance (EPR) spectra were recorded at 300 K with an ESPRIT-425 vol604 spectrometer equipped with an X band (9 GHz microwave frequency). Magnetic susceptibility measurements were conducted with a quantum design superconducting quantum interference device (SQUID magnetometer) over the temperature range 4−300 K, with a magnetic field of 3 kOe.

Electron Microscopy. High-resolution transmission electron microscope images were acquired from powders ultrasonically dispersed in ethanol for 5 min with a drop of suspension deposited on holey carbon-coated copper grids. Data were collected digitally using a JEOL-2100F field emission transmission electron microscope ($C_s = 0.5$ mm and $C_c = 1.1$ mm) operated at 200 kV and fitted with a low-background Gatan double tilt holder and a Si(Li) X-ray detector. As Fe-HAp and Fe-OAp can amorphize after 1−2 min of electron irradiation, the dose was minimized by focusing off-specimen then rapidly translating to the target area.

Biocompatibility. Mouse embryonic fibroblast cells (L929, ATCC) were cultured in Dulbecco's Modified Eagle's Medium (DMEM) supplemented with 10% fetal bovine serum and 1% penicillin-streptomycin and incubated overnight at 37 °C in a humidified (5% CO_2/ 95% air) atmosphere in a T-75 flask. The medium was subsequently aspirated from the flask and washed with a phosphate buffer saline before trypsin-EDTA was added to allow cell detachment. The cells were suspended in a fresh medium and centrifuged to create pellets. The supernatant was discarded and the cell count performed with 20 μL of the cell suspension using a hemacytometer. A 24-well culture plate was used for cell seeding at a density of 3×10^4 cells per well and cultivated in 500 μL of DMEM. The well plate was incubated as before to allow cell attachment, with the medium containing Fe-OAp (0 to 4 mg/mL), which was sterilized under ultraviolet light for 2 h and replaced every two days with total incubation times ranging from 24−168 h.

Cell viability as a function of Fe-OAp was analyzed using Owen's reagent [3-(4,5-dimethylthiazol-2-yl)-5-(3-carboxymethox-

(30) Rodriguez-Lorenzo, L. M.; Hart, J. N.; Gross, K. A. *J. Phys. Chem. B* **2003**, *107*, 8316.

(31) Massiot, D.; Fayon, F.; Capron, M.; King, I.; Le Calvé, S.; Alonso, B.; Durand, J.-O.; Bujoli, B.; Gan, Z.; Hoatson, G. *Magn. Reson. Chem.* **2002**, *40*, 70.

(32) Srinivasan, M.; Ferraris, C.; White, T. J. *J. Solid State Chem.* **2005**, *178*, 2838.

Table 1. The Approximate Phase Boundary of Carbonate Iron Hydroxyapatite (Fe-HAp), Iron Oxyapatite (Fe-OAp), and Tricalcium Phosphate (TCP) Phase Regions as a Function of Iron Loading and Sintering Temperature[a]

Temp	Nominal Fe loading (at%)					
(°C)	0	0.1	0.2	0.3	0.4	0.5
600	29 nm	21 nm	22 nm	17 nm	13 nm	13 nm
700	35 nm	28 nm	33 nm	21 nm		
800	44 nm	48 nm	53 nm			
1000	114 nm	101 nm	116 nm			

Fe-HAp Fe-OAp TCP + Fe-OAp

[a] The crystal domain size as determined by powder X-ray diffraction is given for the single-phase apatite zones.

Table 2. Refined Lattice Parameters (with esds) as a Function of Iron Content for Powders Fired at 600 °C

nominal Fe (x)	a (Å)	c (Å)	volume (Å^3)
0	9.3948(4)	6.8906(4)	526.8
0.1	9.4177(5)	6.8866(5)	529.0
0.2	9.4138(5)	6.8896(5)	528.8
0.3	9.4329(7)	6.8867(7)	530.7
0.4	9.456(1)	6.885(1)	533.2
0.5	9.464(1)	6.879(1)	533.6

yphenyl)-2-(4-sulfophenyl)-2H-tetrazolium] as the inner salt (MTS assay, CellTiter 96 AQ_{ueous} One Solution Cell Proliferation Assay, Promega). This colorimetric method determines the number of metabolically active cells by monitoring the reduction of the tetrazolium salt by dehydrogenase enzymes to a soluble formazan, in the presence of an electron-coupling agent, and measuring the absorbance of formazan (490 nm) directly from the plate. After each incubation interval (24, 72, 120, and 168 h), 100 μL of Owen's reagent was added to the wells and incubated under the same conditions for 4 h prior to transferring the supernatants to a 96-well plate for absorbance readings in a MicroKinetics plate reader (TECAN). The experiment was performed in triplicate for each Fe-HAp concentration. A single-factor analysis of variance was performed to test for statistical significance.

Results

Crystal Chemical Trends. For all Fe-Ap compositions ($0 \le x \le 0.5$), crystallinity was enhanced at elevated sintering temperatures (Table 1). A higher iron content inhibited crystal growth at 600−700 °C, but this effect was not apparent from 800 to 1000 °C, with iron-rich crystals being marginally larger. The HAp-OAp-TCP phase boundaries were dependent on iron loading and heat treatment. The solid solution limit decreased from $x = 0.5$ after firing at 600 °C to $x \sim 0.2$ at 1000 °C. The unit cell expands anisotropically along the a axis with increasing iron loading (Table 2, Figure 3a), with a discontinuity in dilation at $x \sim 0.2$ (Figure 3b) and the appearance of more fully crystalline Fe-OAp (Figure 3c). FTIR spectroscopy shows progressive displacement of hydroxyl (OH^-) and carbonate (CO_3^{2-}) as the iron loading increases, and for $x = 0.5$, these species are at or below the detection limit of this technique (Figure 4a).[33,34] For $x = 0$, the fingerprint bands of OH^- and CO_3^{2-} peaks remain with diminished intensity after acid dissolution, demonstrating that a portion of these species is bound crystallographically (Figure 4b).

Chemical State and Amorphicity. The room-temperature ^{57}Fe−Mössbauer spectrum recorded for Fe-HAp ($x = 0.5$) prepared at 600 °C could be fitted with four quadrupole-split doublets associated with Fe in different sites and environments (Figure 5). The isomer shifts (ISs; relative to α-Fe) and quadrupole splittings (QSs) are presented in Table 3. For all four doublets, the IS value is in the range of 0.27−0.33 mm/s, which is indicative of Fe^{3+} (by contrast, the IS for Fe^{2+} is typically in excess of 1 mm/s). The doublets labeled AA*, BB*, and CC* correspond to the doublets D3 (6-fold coordination), D4 (4-fold coordination), and D5 (surface iron) of reference values (Table 3).[18] The fourth doublet, DD*, provides an approximate description of a weak, broad feature in the shoulders of the spectrum and is attributed to an amorphous phosphate phase. EPR spectra collected from the $x = 0.2$ and $x = 0.5$ materials (also sintered at 600 °C) contain parallel ($g_{||}$) and perpendicular ($g_{\perp}$) components at 8.89 mT and 4.31 mT, which according to Sutter et al.[35] indicates high-spin Fe^{3+} in distorted octahedral or tetrahedral coordination, respectively, although the latter assignment appears crystallochemically unlikely. A broad signal at $g = 2.05$ increases with iron loading and may be due to an amorphous phosphate phase or surface super-paramagnetic Fe^{3+} (Figure 6).[36] The ^{31}P NMR resonance broadened with increasing iron loading in the Fe-HAp region (Figure 7a) primarily due to paramagnetic relaxation, suggesting that Fe^{3+} is in close proximity to the phosphate groups, and possibly suggesting changes in phosphorus coordination.[37] In the Fe-OAp/TCP mixed phase region (Figure 7b), the 800 °C peak is asymmetric on the low frequency side and shifted by about 0.8 ppm, relative to those at 600 and 700 °C, probably as a result of overlapping close-spaced resonances arising from Fe-OAp and TCP that cannot be resolved due to paramagnetic broadening (Table 4). In addition, a broad background appears at 800 °C, which reflects the reconstructive phase transformation of Fe-OAp to TCP and the probable appearance of a transient intermediate amorphous phase.

Quantitative XRD yielded a constant amorphous content in all of the powders independent of iron loading; however, the value obtained (~30 wt %) is an overestimate due to microabsorption.[38] Nonetheless, a non-X-ray diffracting component is significant and was directly identified by electron microscopy (see below). A separate powder neutron

(33) Andres-Verges, M.; Higes Rolando, F. J.; Gonzalez-Diaz, P. F. *J. Solid State Chem.* **1982**, *43*, 237.
(34) Fowler, B. O. *Inorg. Chem.* **1974**, *13*, 194.
(35) Sutter, B.; Wasowicz, T.; Howard, T.; Hossner, L. R.; Ming, D. W. *Soil Sci. Soc. Am. J.* **2002**, *66*, 1359.
(36) Meguro, K.; Ikeya, M. *Jpn. J. Appl. Phys.* **1992**, *31*, 1353.
(37) Sutter, B.; Taylor, R. E.; Hossner, L. R.; Ming, D. W. *Soil Sci. Soc. Am. J.* **2002**, *66*, 455.
(38) De La Torre, A. G.; Bruque, S.; Aranda, M. A. G. *J. Appl. Crystallogr.* **2001**, *34*, 196.

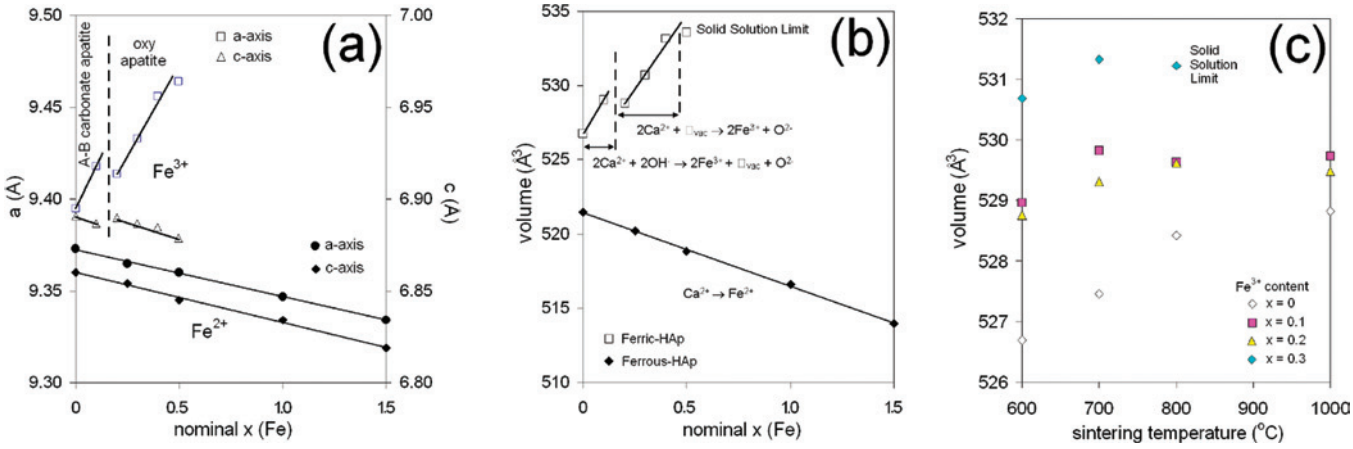

Figure 3. Unit cell trends in Fe-Ap sintered at 600 °C. (a) The incorporation of Fe^{3+} leads to a dilation of the *a* axis indicative of an increase in the volume of the apatite framework. The *c* axis shows a discontinuity at $x \sim 0.2$, reflecting a change in the mechanism of iron incorporation. In contrast, substitution of Fe^{2+} is accompanied by a linear decrease of lattice constants. (b) For the materials sintered at 600 °C, the unit cell volume dilates with Fe^{3+} substitution to a solid solution limit of $x \sim 0.5$, while Fe^{2+} can be accommodated to $x = 1.5$ with a decrease in cell volume.[23] (c) For a given composition of Fe^{3+}-Ap, higher-temperature sintering leads to a slight increase in unit cell volume, especially at low Fe^{3+} loadings.

diffraction investigation is in progress to extract the amorphous component absolutely.

Magnetism. All of the materials were paramagnetic above 100 K, with the degree of magnetization greatest at low iron loadings. In addition, for $x = 0.2$, a transition onset at 90 K appears that may be due to spin coupling combined with crystallochemical modification (Figure 8). Clarification of the origin of this behavior would require additional experiments at different applied magnetic fields, but it is suggested that higher iron levels ($x = 0.3$ onward) lead to clustering of Fe^{3+} that decreases susceptibility, whereas for $x = 0.2$, long-range magnetic ordering is possible.

Nanostructure. The nanostructure of the materials was invariably complex, even for those samples that were nominally single-phase according to XRD. Lattice imaging reveals a combination of crystalline and amorphous regions, where cryptocrystalline agglomerates gradually order as larger acicular HAp and OAp crystals with extension along *c* (Figure 9a). Apatites treated at lower temperatures, and therefore containing more hydroxyl groups, were highly susceptible to damage and rapidly developed etch pits and cavities prior to amorphization (Figure 9b). Large acicular crystals of Fe-OAp proved to be less robust under electron irradiation than equivalent pure HAp. Iron-rich precipitates such as Fe_2O_3 or FeOOH were not detected.

Biocompatibility. The cell viability in Fe-OAp was superior to that in HAp up to concentrations of 4 mg/mL (Figure 10a). The nanoparticles were not cytotoxic, and cell proliferation was significant after 7 days of incubation (Figure 10b).

Discussion

Incorporation of Iron. In $[Ca^{I}_4Ca^{II}_6](PO_4)_6(OH)_2$, the bond valence sum (BVS) of Ca^{I} is 1.97, and that of Ca^{II} is 2.17. In other words, Ca^{I} is marginally underbonded and Ca^{II} somewhat overbonded (Table 5). Introducing Fe^{3+} into HAp without structural relaxation and counterion insertion leads to impossibly low BVSs of 1.12 and 1.23 on the Ca^{I} and Ca^{II} sites, respectively, and consequently, the solid solubility limit of ferric iron is expected to be small. Ferrous iron (Fe^{2+}) is similarly underbonded, even though incorporation is via a straightforward $Ca^{2+} \rightarrow Fe^{2+}$ aliovalent replacement. Khudolozhkin et al.[23] examined ferrous-fluorapatite by X-ray diffraction and showed that Fe^{2+} preferentially displaces Ca^{I} to a solid solution limit of $x = 1.5$ in $[Ca_{10-x}Fe_x^{2+}](PO_4)_6F_2$, confirming that smaller cations generally prefer the metaprismatic site (Figure 3a,b).[39] The unit cell volume decreases with increasing Fe^{2+} content, and because the apatite framework is especially flexible in (001) due to twisting of the metaprisms, it is expected that variation in *a* will greatly exceed the *c* parameter.[7] However, the reported isotropic contraction of the cell edges is at variance with these expected systematics. For both Fe^{2+}- and Fe^{3+}-doped apatites, a detailed analysis of the metaprism twist angles would be helpful to monitor the relative sizes of the framework and tunnel, which in turn provides direct information on the incorporation mechanisms.

In the present study, FTIR showed that, when Fe^{3+} was absent or at low levels (less than $x \sim 0.3$), the materials contained structural carbonate, introduced by the adsorption of atmospheric CO_2, and can be described as mixed A−B-type apatites,[40−42] with carbonate (ideally) distributed over the tunnel (A-type) and framework (B-type) according to coupled substitution:

$$PO_4^{3-} + OH^- \rightarrow 2CO_3^{2-} \quad (1)$$

in a mechanism that also facilitates the altervalent introduction of Fe^{3+}

$$Ca^{2+} + OH^- \rightarrow Fe^{3+} + CO_3^{2-} \quad (2)$$

to yield the formula $[Ca_{10-x}Fe_x][(PO_4)_{6-x+y}(CO_3)_{x+y}]$-$[(CO_3)_y(OH)_{2-y}]$. At the same time, tunnel carbonate and hydroxyl are progressively displaced by O^{2-} to create vacancies.[43]

$$2OH^- + CO_3^{2-} \rightarrow 2O^{2-} + \square_{vac} \quad (3)$$

Beyond $x \sim 0.2$, the A−B hydroxyl and carbonate FTIR signatures become weaker, and Fe^{3+} is then incorporated together with "interstitial" framework oxygen

$$2Ca^{2+} + \square_{Oint} \rightarrow 2Fe^{3+} + O^{2-} \quad (4)$$

While the powder X-ray diffraction data could not confirm this mechanism directly by Fourier mapping, the observation of unit cell dilation with higher ferric iron loadings (Figure 3b) and a simultaneous loss of OH^-/CO_3^{2-} content (Figure 4) is consistent with mechanism 4. An alternative charge balance scheme involving framework A^I vacancies ($3Ca^{2+} \rightarrow 2Fe^{3+} + \square_{AI\ vac}$) is inconsistent with volume expansion.

Framework modification of apatites through the conversion of BO_4 tetrahedra to BO_3 and BO_5 polyhedra is established,[44] with reduced carbonate apatites such as the idealized $[Ca_{10-x}Na_x][(PO_4)_{6-x}(CO_3)_x](OH)_2$ being of particular interest

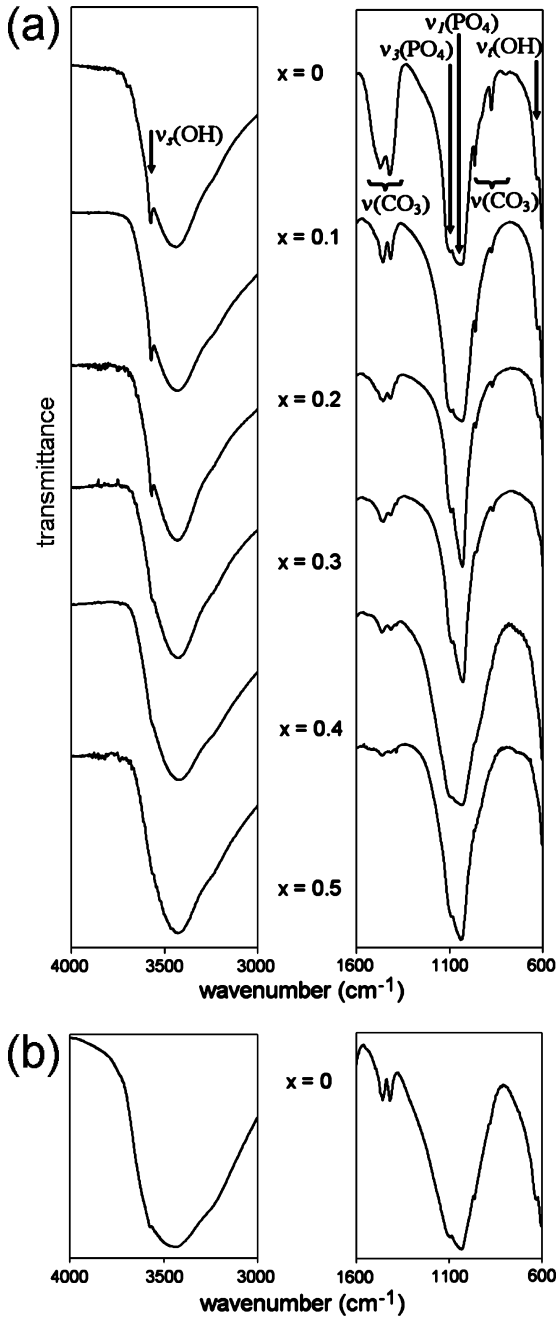

Figure 4. (a) FTIR spectra of Fe-Ap calcined at 600 °C show the signature hydroxyl and carbonate bands of a mixed A−B-type apatite at low iron contents. These features progressively diminish with iron loading because the inclusion of OH^- and CO_3^{2-} operates against the inclusion of the higher-valence Fe^{3+}. (b) After treatment in dilute acid, the hydroxyl and carbonate bands in HAp ($x = 0$) are reduced, showing that these species are both crystallographically incorporated and absorbed. The broad band at ~3450 cm^{-1} is from atmospheric water adsorbed on the KBr specimen pellet.

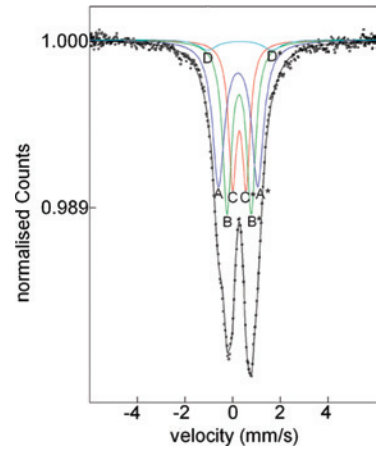

Figure 5. Room-temperature ^{57}Fe−Mössbauer spectrum for Fe-OAp ($x = 0.5$/600 °C) fitted with four quadrupole-split doublets attributed to Fe^{3+} in 6-fold coordination (AA*), 4-fold coordination (BB*), surface iron (CC*), and an amorphous phase (DD*).

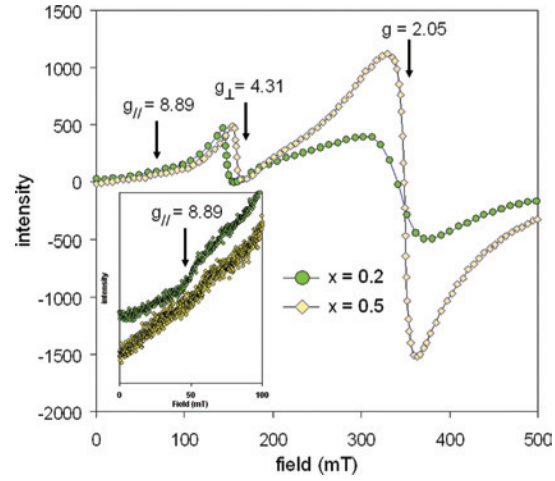

Figure 6. EPR spectra of Fe-Ap ($x = 0.2$ and 0.5) are consistent with Fe^{3+} with the broad feature possibly associated with amorphous material that may be more abundant near the reconstructive HAp to TCP phase boundary.

Table 3. Fitted Parameters of a Four-Doublet-Analysis, Low-Speed ^{57}Fe−Mössbauer Spectrum for Fe-OAp (x=0.5) Sintered at 600 °C

sub spectra	IS (mm/s)	QS (mm/s)	line width (mm/s)	area (%)	possible assignment
AA*	0.33(6)	1.65(23)	0.60(20)	37.7	Fe^{3+} in A^I
BB*	0.27(4)	1.02(16)	0.45(7)	33.8	Fe^{3+} in A^{II}
CC*	0.28(7)	0.57(10)	0.4	24.7	surface Fe^{3+}
DD*	0.30(7)	2.7(1.3)	0.9(4)	3.9	amorphous Fe^{3+}

(39) Pan, Y.; Fleet, M. E. *Rev. Mineral. Geochem.* **2002**, *48*, 13–50.
(40) Fleet, M. E.; Liu, X. *J. Solid State Chem.* **2003**, *174*, 412.
(41) Fleet, M. E.; Liu, X. *J. Solid State Chem.* **2004**, *177*, 3174.
(42) Fleet, M. E.; Liu, X. *Biomaterials* **2005**, *26*, 7548.
(43) Elliot, J. C.; Mackie, P. E.; Young, R. A. *Science* **1973**, *180*, 1055.
(44) Pramana, S. S.; Klooster, W. T.; White, T. J. *J. Solid State Chem.* **2008**, *181*, 1717.

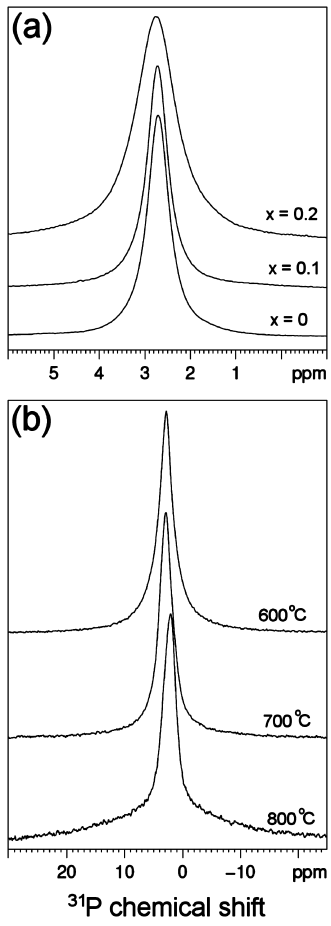

Figure 7. ^{31}P MAS NMR spectra of (a) Fe-Ap sintered at 800 °C as a function of iron loading, showing the progressive broadening of the phosphorus resonance due to a combination of paramagnetic effects and the partial conversion of PO_4 tetrahedra to PO_5 trigonal bipyramids that accompanies the replacement of Ca^{2+} by Fe^{3+}, and (b) the asymmetric broadening arising from overlapping signals from Fe-OAp ($x = 0.5$) mixed with TCP that becomes more evident at higher temperatures as the phase transformation proceeds.

Table 4. Fitted Parameters of Experimental ^{31}P NMR Peaks Recorded at 10 kHz for Pure HAp and Fe-OAp ($x = 0.4$ and 0.5) Sintered at 800 °C

x	shift (Hz)	width (Hz)	$xG/(1-x)L$	integrated (%)	assignment
0	438	95	0	100	Fe-HAp
0.4	425	430	0.4	37.0	Fe-HAp
	520	3000	0.0	63.0	TCP
0.5	324	330	0.4	31.5	Fe-HAp
	520	37	0.9	10.5	TCP
	560	2800	0.0	58.0	

in osteolgy.[45] Oxidized apatites such as $[La_{10}][(GeO_4)_5(GeO_5)]O_2$ are under development as fuel cell electrolytes.[46] Therefore, it is reasonable to suppose that Fe-OAp prepared under conditions where mechanism 4 is significant will lead to the transformation of some of PO_4 tetrahedra to PO_5 trigonal bipyramids, a common coordination figure for phosphorus, and a crystallochemical formula for carbonate-free Fe-Ap best represented as $[Ca_{10-x}Fe_x^{3+}][(PO_4)_{6-x/2}(PO_5)_{x/2}][(OH)_{2-y}O_{2y}]$. This substitution can continue until $x = 0.5$, and at the lowest sintering temperature (600 °C), single-phase apatite was produced to this putative limit. The $(PO_4)^{3-}$ and $(PO_5)^{5-}$ phosphate ions will have distinct ^{31}P resonances that can in principle be differentiated by NMR (Figure 6a), but in practice, the relatively low PO_5 concentration combined with the strong paramagnetic broadening induced by Fe^{3+} masked this fine feature. An indirect means to confirm the appearance of PO_5 would be to dope HAp with nonmagnetic trivalent cations such as Sc^{3+} (IR = 0.745Å) or Ga^{3+} (IR = 0.62Å) that should mimic the behavior of iron.

The partitioning of Fe^{3+} over the A^I and A^{II} crystallographic sites remains to be resolved. As noted earlier, small cations generally favor the metaprismatic A^I site, while species of formal valence >2 are driven toward the A^{II} site where a larger number of near neighbors disperse charge more evenly. Jiang et al.,[18] using a combination of EPR and Mössbauer spectroscopies, concluded that Fe^{3+} was preferentially located at the A^I site of Fe-HAp with a charge balance accommodated by the creation of Ca^{II} and hydroxyl vacancies ($2Ca^{2+} + OH^- \rightarrow Fe^{3+} + \square_{Ca} + \square_{OH}$). However, in the present case, this mechanism would be inconsistent with unit cell dilation in tandem with increasing iron content. It is noted that Jiang et al. also reported *a*-edge expansion ($a = 9.4223$ Å and $c = 6.8764$ Å), suggesting their material may also have been an oxyhydroxapatite (see Table 2). In these experiments, Rietveld analysis could not refine the occupation of Fe^{3+} over the calcium sites, although least-squares fitting invariably yielded a scattering power of more than 18 electrons (i.e., Ca^{2+}) on both A positions, and Mössbauer and EPR spectroscopy contained multiple components suggestive of a distributed iron content (Figure 4 and Figure 5).

HAp is trimorphic and may adopt $P6_3/m$, $P\bar{1}$, or $P112_1/b$[43,47,48] symmetry, with the latter assignment being a reasonable approximation of incommensurate hydroxyl order.[49] The symmetry hierarchy of apatites shows that $P6_3$, $P\bar{3}$, $P\bar{6}$, and $P2_1/m$ are maximal nonisomorphic subgroups of $P6_3/m$, while $P2_1$ and $P\bar{1}$ are similarly related to $P2_1/m$ (Figure 11), and can arise from topological distortion of the framework,[50] cation ordering,[7] or the incorporation of interstitial oxygen.[46] However, $P112_1/b$ is distinct in the sense that it represents an average structure with splitting of the tunnel anion site. The presence of PO_5 polyhedra or tunnel nonstoichiometry makes it likely that $P6_3/m$ is an approximation of Fe-Ap symmetry, and further examination by neutron diffraction or single-crystal X-ray diffraction will be required to establish the true symmetry—for example, $Ca_{10}(PO_4)_6(OH)_{2-x}O_{x/2}$ ($0.78 < x < 1.56$)[47] is triclinic $P\bar{1}$ and $Ca_{10}(PO_4)_6(CO_3)_xO_{2-2x}$ type-A carbonate apatite is hexagonal $P\bar{3}$.[40] In the case of natural ferrous apatites, a single-crystal investigation by Hughes et al.[51] found that small amounts

(45) Wilson, R. M.; Elliot, J. C.; Dowker, S. E. P.; Smith, R. I. *Biomaterials* **2004**, *25*, 2205.
(46) Pramana, S. S.; Klooster, W. T.; White, T. J. *Acta Crystallogr., Sect. B* **2007**, *63*, 597.
(47) Adolfson, E.; Grins, J.; Fitch, A. *J. Mater. Sci.* **2001**, *36*, 663.
(48) Mercier, P. H. J.; Le Page, Y.; Whitfield, P. S.; Mitchell, L. D. *J. Appl. Crystallogr.* **2006**, *39*, 369.
(49) McCubbin, F. M.; Mason, H. E.; Park, H.; Phillips, B. L.; Parise, J. B.; Nekvasil, H.; Lindsley, D. H. *Am. Mineral.* **2008**, *93*, 210.
(50) Baikie, T.; Mercier, P. H. J.; Elcombe, M. M.; Kim, J. Y.; Le Page, Y.; Mitchell, L. D.; White, T. J.; Whitfield, P. S. *Acta Crystallogr., Sect. B* **2007**, *63*, 251.
(51) Hughes, J. M.; Fransolet, A. M.; Schreyer, W. *N. Jb. Miner. Mh.* **1993**, *11*, 504.

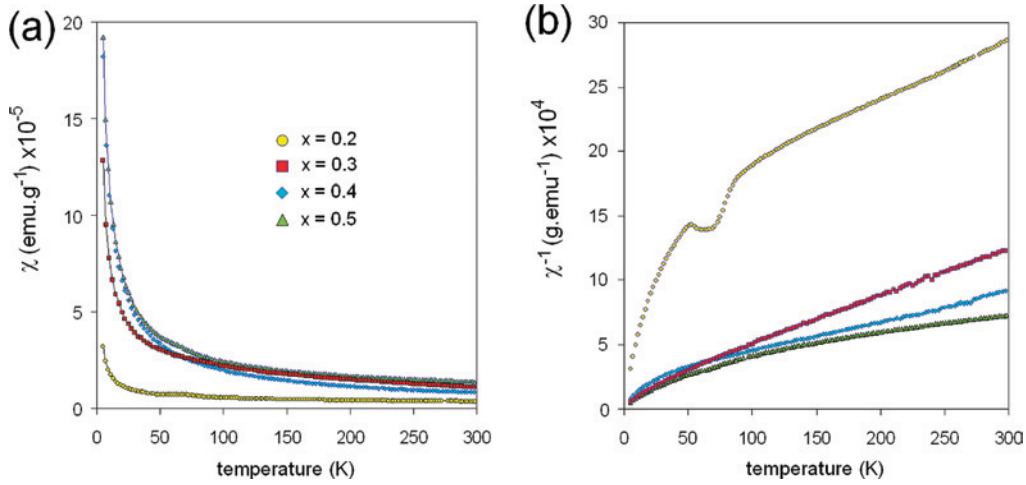

Figure 8. The (a) magnetic susceptibility (χ) and (b) inverse magnetic susceptibility (χ^{-1}) versus temperature in a magnetic field of 3 kOe, typical of paramagnetism above 100 K. A transition with an onset at 90 K reflects a change in spin order associated with a crystallographic phase transition (see Figure 3).

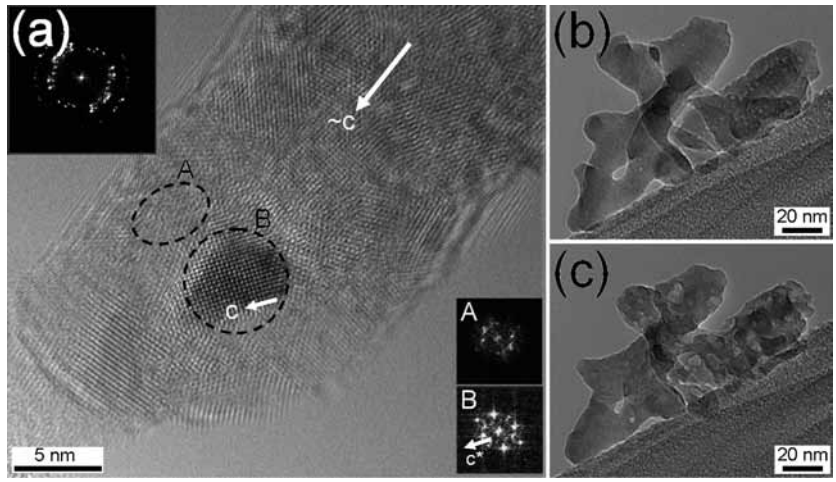

Figure 9. (a) Lattice image of Fe-OAp ($x = 0.5$ sintered at 600 °C) showing distinctive amorphous (region A) and crystalline (region B) areas collected using the low electron dose technique. The fast Fourier transform (FFT) of the whole image is shown on the top left, while local order within the outlined regions is illustrated on the bottom right. The nanocrystal (B) is in the [100] orientation. The developing acicular morphology with extension along $\sim c$ is evident, and as annealing continues, the small domains become increasingly coherent. In general, electron beam damage was rapid, as shown by the bright field images for a collection of Fe-OAp crystals collected after (b) 1 min and (c) 3 min irradiation.

of iron lead to a $P2_1/m$ structure. [Preliminary analysis of powder neutron diffraction data for the iron-apatites used in this study has conclusively shown that the lattice metric departs from hexagonal at higher iron loadings.]

Magnetic Properties. The magnetic phase transition observed at a low iron content ($x = 0.2$) has not been observed previously in apatite and not only reflects modification of the spin order but also the crystallochemical conversion from a type A−B apatite to an oxidized structure with framework oxygen, and an accompanying change in symmetry. The proximity of Fe^{3+} to the charge-balancing PO_5 groups is unknown, and clustering of these species should be examined by temperature-dependent Mössbauer, NMR, and EPR spectroscopy. Nonetheless, it is clear that neither Fe-HAp nor Fe-OAp is strongly magnetic and will not intrinsically contribute to the functionality of biomagnetic nanoparticles, where superparamagnetism is essential to control placement by an external field. Rather, apatites must be prepared as composites with hematite[29] or exploit surface sorbed iron.[28,52] The contribution from amorphous phosphates to overall magnetism could not be assessed quantitatively.

Toxicity and Functionality. Fe-OAp is biocompatible, and the enhanced viability of embryonic fibroblast cells, compared to pure HAp, shows potential for hastening bone growth and preventing dental caries.[53,54] Moreover, the high amorphicity and small crystallite size of Fe-OAp may be advantageous for biomedical applications requiring a high surface area and activity in body fluids.[55,56] Bone regeneration scaffolds and orthopedic filler materials could be fabricated from Fe-OAp and incorporated in glass ceramics or calcium phosphate cements as the growth of osteoblast

(52) Guo, Y.; Zhou, Y.; Jia, D.; Meng, Q. *Acta Biomater.* **2008**, in press.
(53) Tanizawa, Y.; Sawamura, K.; Suzuki, T. *J. Chem. Soc., Faraday Trans.* **1990**, *86*, 1071.
(54) Leventouri, Th. *Biomater. Res. Adv.* **2007**, 145–182.
(55) Ong, H. T.; Loo, J. S. C.; Boey, F. Y. C.; Russell, S. J.; Ma, J.; Peng, K. W. *J. Nanopart. Res.* **2008**, *10*, 141.
(56) Xu, Q.; Tanaka, Y.; Czernuszka, J. T. *Biomaterials* **2007**, *28*, 2687.

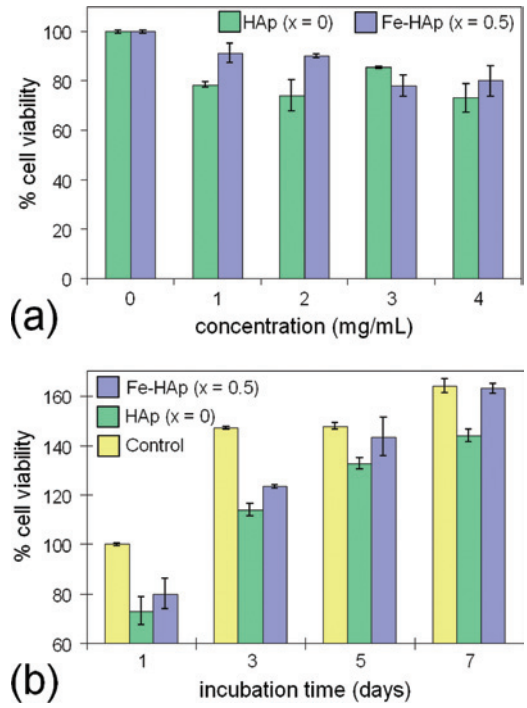

Figure 10. L929 fibroblast cell viability as a function of (a) the concentration of pure HAp and Fe-OAp ($x = 0.5$) sintered at 600 °C and (b) the incubation period.

Table 5. Bond Valence Sums for Iron Incorporation in the HAp Structure without Relaxation or the Insertion of Oxygen[a]

coordination polyhedron	bond lengths (Å)	partial bond valence Ca^{2+}	partial bond valence Fe^{3+}	partial bond valence Fe^{2+}
A^I	3 × 2.404	0.307	0.175	0.164
	3 × 2.475	0.253	0.144	0.135
	3 × 2.841	0.094	0.054	0.050
BVS		**1.96**	**1.12**	**1.05**
A^{II}	2 × 2.336	0.369	0.210	0.197
	2 × 2.426	0.289	0.165	0.154
	2 × 2.551	0.206	0.118	0.110
	1 × 2.397	0.312	0.178	0.167
	1 × 2.748	0.121	0.069	0.065
BVS		**2.16**	**1.23**	**1.15**

[a] The bond lengths were calculated from the data of Rodriguez-Lorenzo et al.,[30] and the bond valence parameters for the calculation were taken from Brown and Altermatt.[60]

cells would be favorable.[57] It is clear that the surface chemistry of Fe-OAp is quite distinct from that of HAp, as evidenced by the different capacities to adsorb hydroxyl/carbonate (Figure 4), and this property might be used to control the loading and release of drugs.[58,59]

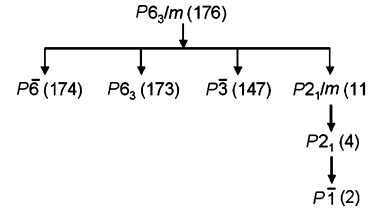

Figure 11. Space group hierarchy for apatites.

Conclusion

Ferric iron is incorporated in HAp by replacing calcium. At low Fe^{3+} loadings ($x < 0.2$), charge balance is maintained through the inclusion of tunnel carbonate, introduced via atmospheric CO_2, which displaces hydroxyl and yields the ideal phase $[Ca_{10-x}Fe_x][(PO_4)_{6-x+y}(CO_3)_{x+y}][(CO_3)_y(OH)_{2-y}]$. At higher Fe^{3+} contents ($x \geq 0.2$), CO_2 uptake is less significant, and the oxyapatite $[Ca_{10-x}Fe_x^{3+}][(PO_4)_{6-x/2}(PO_5)_{x/2}][(OH)_{2-y}O_{2y}]$ is stabilized with partial conversion of the PO_4 tetrahedra to PO_5 polyhedra. Spectroscopic and crystallographic evidence suggests that Fe^{3+} is distributed over the A^I and A^{II} sites; however, the partitioning coefficient remains to be determined, as does the symmetry of Fe-OAp. The possible role of A site nonstoichiometry, and the nature of the reconstructive transformation to TCP at higher sintering temperatures and iron loadings, is incompletely understood.

Fe-OAp shows enhanced excipient behavior compared to HAp but is weakly paramagnetic and not intrinsically suitable for localized hyperthermic therapies. By focusing on crystal chemistry, this investigation complements earlier studies that examined surface adsorption of iron oxides (e.g., Fe_3O_4) or oxyhydroxides (e.g., FeOOH).[20,23−26,28,29] Furthermore, controlling the abundance and composition of amorphous material residing at crystalline interfaces will underpin the design of hybrid architectures, such as core−shell Fe_3O_4−Fe-HAp nanopebbles for drug delivery or contrast agents in magnetic resonance imaging and biosensors.[58,59]

IC801491T

(57) Balasundaram, G.; Sato, M.; Webster, T. J. *Biomaterials* **2006**, *27*, 2798.
(58) Arruebo, M.; Fernandez-Pacheco, R.; Velasco, B.; Marquina, C.; Arbiol, J.; Irusta, S.; Ibara, R. M.; Santamaria, J. *Adv. Funct. Mater.* **2007**, *17*, 1473.
(59) Wuang, S. C.; Neoh, K. G.; Kang, E.-T.; Pack, D. W.; Leckband, D. E. *Adv. Funct. Mater.* **2006**, *16*, 1723.
(60) Brown, I. D.; Altermatt, D. *Acta Crystallogr., Sect. B* **1985**, *41*, 244.